BIOCHEMISTRY
including biophysical chemistry & molecular biology
Article

Biochemistry **2010,** *49,* 6953–6962 6953
DOI: 10.1021/bi1006089

Redox-Dependent Domain Rearrangement of Protein Disulfide Isomerase from a Thermophilic Fungus†

Masayoshi Nakasako,*[,‡,§] Aya Maeno,[∥] Eiji Kurimoto,[∥,⊥] Takushi Harada,[∥] Yoshiki Yamaguchi,[∥,#] Toshihiko Oka,[‡] Yuki Takayama,[‡,§] Aya Iwata,[‡,§] and Koichi Kato[∥,△]

[‡]*Department of Physics, Faculty of Science and Technology, Keio University, 3-14-1 Hiyoshi, Kouho-ku, Yokohama 223-8522, Japan,* [§]*The RIKEN Harima Institute/SPring-8, Sayo, Hyogo 679-5148, Japan,* [∥]*Graduate School of Pharmaceutical Sciences, Nagoya City University, 3-1 Tanabe-dori, Mizuho-ku, Nagoya 467-8603, Japan,* [⊥]*Faculty of Pharmacy, Meijo University, 150 Yagotoyama, Tempaku-ku, Nagoya 468-8503, Japan,* [#]*Structural Glycobiology Team, Systems Glycobiology Research Group, Chemical Biology Department, Advanced Research Institute, RIKEN, 2-1 Hirosawa, Wako-shi, Saitama 351-0198, Japan, and* [△]*Okazaki Institute for Integrative Bioscience and Institute for Molecular Science, National Institutes of Natural Sciences, 5-1 Higashiyama, Myodaiji, Okazaki, Aichi 444-8787, Japan*

Received April 20, 2010; Revised Manuscript Received July 6, 2010

ABSTRACT: Protein disulfide isomerase (PDI) acts as folding catalyst and molecular chaperone for disulfide-containing proteins through the formation, breakage, and rearrangement of disulfide bonds. PDI has a modular structure comprising four thioredoxin domains, ***a***, ***b***, ***b***′, and ***a***′, followed by a short segment, ***c***. The ***a*** and ***a***′ domains have an active site cysteine pair for the thiol−disulfide exchange reaction, which alters PDI between the reduced and oxidized forms, and the ***b***′ domain provides a primary binding site for substrate proteins. Although the structures and functions of PDI have studied, it is still argued whether the overall conformation of PDI depends on the redox state of the active site cysteine pair. Here, we report redox-dependent conformational and solvation changes of PDI from a thermophilic fungus elucidated by small-angle X-ray scattering (SAXS) analysis. The redox state and secondary structures of PDI were also characterized by nuclear magnetic resonance and circular dichroic spectroscopy, respectively. The oxidized form of PDI showed SAXS differences from the reduced form, and the low-resolution molecular models restored from the SAXS profiles differed between the two forms regarding the positions of the ***a***′−***c*** region relative to the ***a***−***b***−***b***′ region. The normal mode analysis of the crystal structure of yeast PDI revealed that the inherent motions of the ***a***−***b***−***b***′ and ***a***′−***c*** regions expose the substrate binding surface of the ***b***′ domain. The apparent molecular weight of the oxidized form estimated from SAXS was 1.1 times larger than that of the reduced form, whereas the radius of gyration (ca. 33 Å) was nearly independent of the redox state. These results suggest that the conformation of PDI is controlled by the redox state of the active site cysteine residues in the ***a*** and ***a***′ domains and that the conformational alternation accompanies solvation changes in the active site cleft formed by the ***a***, ***b***, ***b***′, and ***a***′ domains. On the basis of the results presented here, we propose a mechanism explaining the observed redox-dependent conformational and solvation changes of PDI.

Protein disulfide isomerase (PDI,[1] EC 5.3.4.1) (*1*−*5*) is one of the folding catalysts existing in the lumen of the endoplasmic reticulum, which is a specialized compartment for the folding of secretory proteins. PDI introduces disulfide bonds in substrate proteins (oxidase activity) and catalyzes the rearrangement of incorrect disulfides (isomerase activity) during the process of protein folding and is thought to act also as a chaperone independent of its isomerase activity (*6*, *7*).

PDI is a member of the thioredoxin superfamily (*8*, *9*) and has a modular structure comprising four domains of the thioredoxin fold, ***a***, ***b***, ***b***′, and ***a***′, followed by a short segment, ***c*** (*10*−*17*) (Figure 1A). The ***b***′ and ***a***′ domains are connected by a flexible ***x***-linker region composed of ca. 20 amino acid residues. Nonequivalent functional roles of the four structurally homologous domains have been revealed through biochemical and mutagenesis studies (*18*−*20*). The ***a*** and ***a***′ domains each contain a WCGHCK active site sequence motif that is directly involved in the thiol exchange reaction (*8*, *11*) (Figure 1A). The cysteine pair in this motif exists as an intramolecular disulfide that catalyzes disulfide formation in substrate proteins under oxidizing conditions (oxidized form) or exists in the dithiol state to assist the isomerization of disulfides in substrates under reducing conditions (reduced form). For instance, the ***a*** and ***a***′ domains in

†SAXS experiments were performed with the approval of the Japan Synchrotron Radiation Research Institute (Proposal No. 2005B0380). This research was supported by Grants-in-Aid from the MEXT Japan to M.N. (No. 15076210, No. 20050030, and No. 22018027) and K.K. (No. 15032249, No. 20059030, No. 20107004, and No. 21370050) and from the JSPS Japan to M.N. (No. 19204042 and No. 22244054). This project was supported by the Protein 300 Project and Nanotechnology Project from the MEXT and by the NINS Cooperative Project Biomolecular Sensor and the Joint Studies Program of the Institute for Molecular Science of the National Institute of Natural Sciences.

*Address correspondence to this author: phone, (81)-45-566-1713; fax, (81)-45-566-1672; e-mail, nakasako@phys.keio.ac.jp.

[1]Abbreviations: *β*-ME, *β*-mercaptoethanol; CD, circular dichroism; DTT, dithiothreitol; NMR, nuclear magnetic resonance; PDI, protein disulfide isomerase; PDI_{ox}, oxidized form of recombinant protein disulfide isomerase from *H. insolens*; PDI_{red}, reduced form of protein disulfide isomerase from *H. insolens*; R_g, radius of gyration; SAXS, small-angle X-ray scattering.

Published on Web 07/12/2010

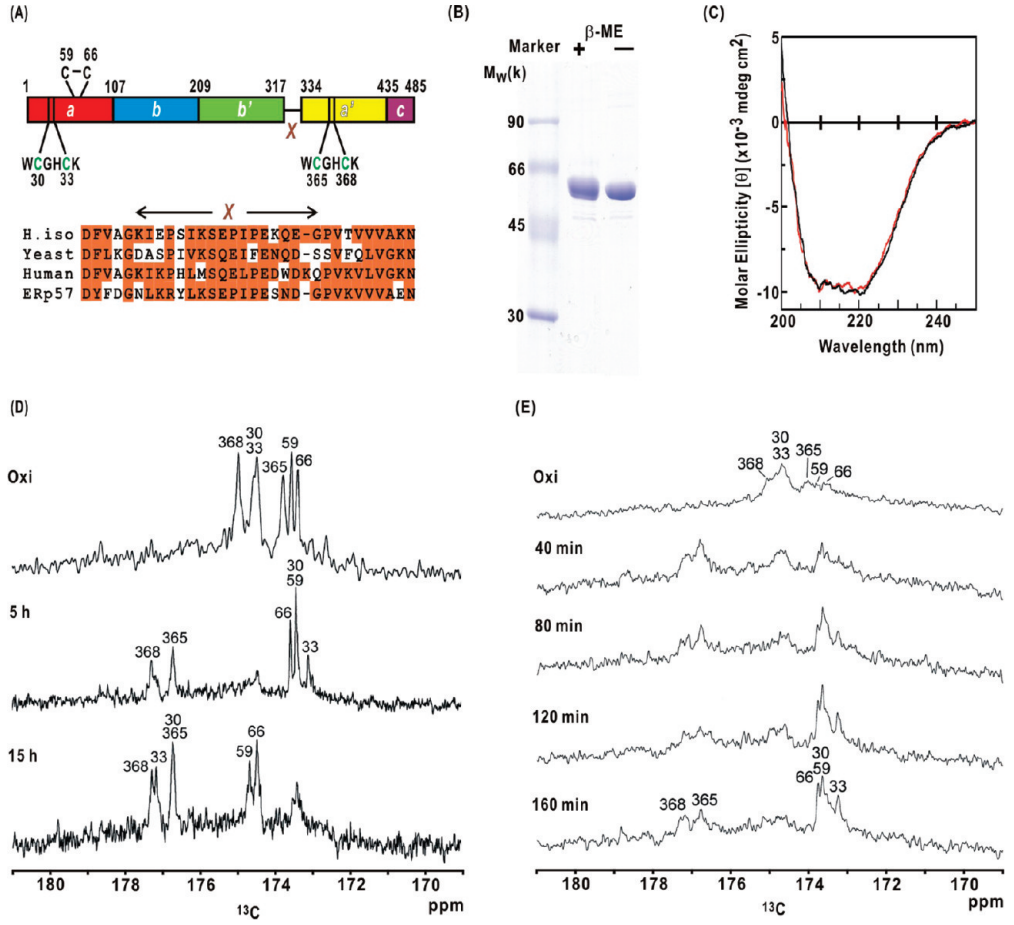

FIGURE 1: (A) A schematic diagram of domain organization in PDI from *H. insolens* based on the amino acid sequences (*26*) and structural studies on the ***a***−***b*** and ***b***′−***X***−***a***′ fragments (*17*). The four thioredoxin domains (***a***, ***b***, ***b***′, and ***a***′) and the C-terminal short segment ***c*** are shown as colored boxes. Active site sequences and a structural disulfide between residues 59 and 66 in domain ***a*** are indicated. An alignment of the amino acid sequences of the ***x***-linker regions (***X***) is shown for *H. insolens* (*26*), yeast (*14*), and human (*42*) PDIs and human ERp57 (*34*). The orange background indicates residues that are highly conserved between the four proteins. (B) SDS−PAGE patterns of PDI after a week-long incubation in oxidizing buffer. The sample solutions were prepared in the presence (indicated by the symbol "+" above the lanes) and the absence (−) of β-ME before the SDS treatment. The M_ws of marker proteins are indicated to the left of the gel. (C) CD spectra of PDI_{red} (red line) and PDI_{ox} (black). (D) ^{13}C NMR spectra of PDI selectively labeled with ^{13}C at the carbonyl carbon atoms of cysteine residues. Spectra (from the top to the bottom) correspond to PDI_{ox}, and PDI reduced by 2 mM DTT for 5 and 15 h, respectively. (E) ^{13}C NMR spectra of PDI_{ox} (top) and PDI incubated with 10 mM DTT for 40, 80, 120, and 160 min. The assigned residue numbers are indicated at the top of the peaks in (D) and (E).

yeast PDI are thought to serve opposing functional roles as a disulfide isomerase and oxidoreductase, respectively, based on the study of disulfide bond formation in a reaction driven by the natural oxidant Ero1p (*21*). The ***b*** and ***b***′ domains share no obvious sequence identity with the ***a*** and ***a***′ domains (*8*) and are redox inactive due to the lack of the active site sequence motif. Although the ***b***′ domain is considered to act as the principal peptide-binding platform (*17*, *19*, *22*), all domains of the thioredoxin fold are necessary for the complete binding of polypeptides, including non-native proteins (*20*, *23*).

The crystal structure of yeast PDI at 277 K (*14*) has provided a structural framework to help to understand the action mechanisms of this modular enzyme. The four thioredoxin domains are arranged in a twisted "U" shape with the active sites of the ***a*** and ***a***′ domains facing each other. The inside surface of the "U" is enriched with hydrophobic residues from the ***b***′ domain, which are considered to be essential for interactions with substrate proteins. In addition, the inherent flexibility of yeast PDI has been demonstrated by the crystal structure at 298 K (*15*), which displays a rearrangement of the ***a*** and ***a***′ domains from the 277 K structure. Despite the fact the structures and functions of PDI have been well studied, it is unclear whether the conformation of PDI is redox dependent.

Although a study has suggested that yeast PDI acts as a redox-dependent chaperone for the unfolding of the cholera toxin A1 fragment (*24*), the redox dependence of the PDI conformation is still controversially argued (*25*). The arrangement of the domains in yeast PDI depends on the temperature and crystallization conditions (*14*, *15*), and the oxidized form of yeast PDI is more sensitive to protease digestion than the reduced form (*24*). In the thermophilic fungus *Humicola insolens*, the ***b***′−***X***−***a***′ fragment of PDI displays a rearrangement of the ***b***′ and ***a***′ domains that exposes the substrate binding hydrophobic surface of the ***b***′ domain upon oxidation of the ***a***′ active site (*17*). These findings suggest the possibility that domain rearrangements are dependent on the redox state of the active sites. Thus, further structural investigations are necessary to understand the mechanisms in the redox-dependent function of PDI.

In an effort to understand further the redox-dependent conformational changes of PDI, we conducted small-angle X-ray scattering (SAXS) analyses of *H. insolens* PDI. SAXS is advantageous for the control of active site redox states through the exchange of buffer solutions and provides structural information without influences from molecular packing in crystals. The observed SAXS profiles of PDI samples, which were characterized

by nuclear magnetic resonance (NMR), circular dichroic (CD) spectroscopy, and biochemical assays, demonstrated a redox-dependent rearrangement of the ***a′*−*c*** region relative to the ***a*−*b*−*b′*** region accompanying solvation changes.

MATERIALS AND METHODS

Preparation of Full-Length PDI. PDI (residues 1−485) from *H. insolens* was overexpressed with an N-terminal hexahistidine tag using *Escherichia coli* strain BL21(DE3), as described previously (*26*, *27*), and was free from N-glycosylation. Tagged PDI was purified using a chelating Sepharose fast-flow column (Amersham Biosciences, Sweden), and the tag was then removed by a 24 h incubation in the presence of factor Xa (Amersham Biosciences). The sample solution was dialyzed against 50 mM Tris-HCl buffer (pH 8.0), and further purification was performed by ion-exchange chromatography using a Resource Q column (Amersham Biosciences).

Sample Buffer Used in the Structural Study. Prior to performing structural analyses, we measured SAXS profiles and CD spectra of the prepared PDI in four types of buffers (Supporting Information Figures S1 and S2). Among the buffers tested, we found that the 10 mM HEPES buffer containing 100 mM KCl (pH 6.0) was the most suitable for SAXS analysis, as PDI displayed very little aggregation in this buffer. Although the buffer action of HEPES was marginal, the acidic condition was necessary to suppress the reduction of the structural disulfide formed by the pair of Cys59 and Cys66, which correspond to Cys90 and Cys97 in yeast PDI (*28*). The solution stabilized the PDI molecule without any adduct formation in the active site cysteine residues and displayed very little drift in the pH.

Preparation of PDI in the Oxidized and Reduced Forms. Following the initial purification, PDI was fully oxidized by dialyzing against 50 mM Tris-HCl buffer (pH 8.0) containing 100 mM KCl and 0.1 mM oxidized glutathione at 277 K for 1 week. This unusually long period of incubation was necessary because the oxidation of the active sites in thermophilic *H. insolens* PDI proceeded more slowly than those of yeast and human PDI. After the incubation, the sample solution was purified further by ion-exchange chromatography to exclude any contaminants appearing during the incubation period. The purified PDI was concentrated in 10 mM HEPES buffer containing 100 mM KCl (pH 6.0) by ultrafilteration.

PDI in the reduced form was prepared simply by adding DTT at a final concentration of 10 mM to the solution of PDI in the oxidized form immediately after being purified by ion-exchange chromatography. SAXS, CD, and NMR measurements for PDI under reducing buffer conditions were performed after more than a 40 min incubation of the PDI−DTT mixture (see the Results section).

The apparent molecular weights (M_ws) of PDI in the reducing and oxidizing buffers were measured by size-exclusion chromatography. Sodium dodecyl sulfate−polyacrylamide gel electrophoresis (SDS−PAGE) was used to analyze the samples prepared in the presence and the absence of 2 mM β-mercaptoethanol (β-ME).

Nuclear Magnetic Resonance Spectroscopy. One-dimensional ^{13}C NMR spectra of PDI were measured at 310 K on an AMX400 spectrometer (Bruker Biospin) as described previously (*29*), using a 100 mm NMR sample tube filled with 12.5 mg/mL PDI dissolved in 10 mM sodium phosphate buffer containing 100 mM KCl and 0.05% (w/v) NaN_3 (pH 7.3). The active site and structural disulfides were reduced more rapidly under this solvent condition than the buffer used for SAXS measurements (described below). The purpose of the NMR measurement was the assignments of the observed carbonyl ^{13}C signals by combining the double-labeling method and the spectral comparison between full-length PDI and its ***a*−*b*** and ***b′*−*X*−*a′*** fragments obtained in a previous study (*17*). Each ^{13}C NMR spectrum was collected for 5 h to obtain good signal-to-noise ratio for unambiguous assignments.

A time-course NMR analysis of PDI was carried out to determine the redox state of the active site and structural disulfides of PDI under the identical solvent conditions used in the SAXS experiments. The PDI sample (25 mg/mL) was dissolved in 10 mM HEPES buffer containing 100 mM KCl and 0.05% (w/v) NaN_3 (pH 6.0), and one-dimensional ^{13}C NMR spectra were measured at 303 K on an Avance 600 spectrometer equipped with a TCI cryogenic probe (Bruker Biospin). After the addition of 10 mM DTT, ^{13}C NMR spectra were successively collected every 40 min. The assignments of observed carbonyl ^{13}C signals were performed by comparing the results with the NMR experiment described above.

CD Spectroscopy Measurements. CD spectra in the region of 200−250 nm were measured for PDI samples of 0.1 mg/mL in 10 mM HEPES buffer containing 100 mM KCl (pH 6.0) using a J-725 spectropolarimeter (JASCO) at 293 K. The spectra of buffer solutions were subtracted from those of the sample solutions.

SAXS Experiments. SAXS data were collected at the BL40B2 of the SPring-8 (Hyogo, Japan) according to the procedure described previously (*30*). The X-ray wavelength was 1.0000 Å, and an R-AXIS IV^{++} system (Rigaku, Japan) was used as the detector at a camera distance of 1000 mm. The exposure time was 60 s, and the temperature of samples was maintained at 298 K. The concentration of the PDI solution was less than 10 mg/mL in 10 mM HEPES buffer containing 100 mM KCl (pH 6.0). PDI in the reduced form was prepared as described above 40 min prior to the measurements. SAXS of hen egg white lysozyme (M_w of 14300; Sigma) were also collected as a reference for determining the apparent M_w of PDI. The SDS−PAGE for X-ray-exposed samples indicated that a 60 s exposure caused very little radiation damage.

SAXS Analysis. Two-dimensionally recorded SAXS patterns were reduced to one-dimensional profiles after subtracting the background scattering of the buffer solution. SAXS profiles in the small-angle region were analyzed by Guinier's approximation (*31*). The scattering intensity $I(S,C)$ at a scattering vector S and a protein concentration C was approximated using the forward scattering intensity $I(S = 0,C)$ and the radius of gyration $R_g(C)$ as

$$I(S,C) = I(S = 0,C) \exp[(-4\pi^2/3)R_g(C)^2S^2] \quad S = 2 \sin \theta/\lambda$$

where 2θ is the scattering angle and λ is the wavelength of the X-ray.

Under diluted conditions, the concentration dependencies of $I(S = 0,C)$ and $R_g(C)^2$ were approximated as

$$KC/I(S = 0,C) = 1/M_w + 2A_2C$$

$$R_g(C)^2 = R_g(C = 0)^2 - B_{if}C$$

where K is a constant, M_w is the apparent molecular weight of a protein, A_2 is the second virial coefficient, and B_{if} reflects the interprotein interactions (*31*). Attractive interaction results in

negative A_2, whereas repulsive ones give positive values. The sign of B_{if} is identical to that of A_2. Assuming a partial specific volume of 0.74 cm^3/g for soluble proteins, the apparent M_w of a protein can be determined by $I(S = 0,C = 0)$ of a reference protein (lysozyme) with a known M_w.

The intensity profiles in $S < 0.01$ Å^{-1} were extrapolated to the infinite dilution limit to correct for the concentration effects on the scattering profiles. The corrected profiles were merged with the profile in $S > 0.01$ Å^{-1} measured from a 10 mg/mL PDI solution. The distance-distribution function $P(r)$ was then calculated for the merged profiles using the program GNOM (*32*).

The program GASBOR (*33*) was used to restore the low-resolution molecular models of PDI from the corrected SAXS profiles as an assembly of small spheres called dummy residues. GASBOR minimizes the discrepancy between the experimental and calculated scattering profiles by keeping a compactly interconnected configuration of the dummy residues approximating the molecular shape. The discrepancy in intensity was monitored with the χ^2 value defined as

$$\chi^2 = 1/(N-1)\sum_j \{[c(S_j)I_{\mathrm{exp}}(S_j) - KI_{\mathrm{model}}(S_j)]/\sigma(S_j)\}^2$$

where N is the number of experimental data points, S_j is the scattering vector of the jth data point, $c(S_j)$ is a correction factor, K is a scale factor, and $\sigma(S_j)$ is the statistical error in the experimental scattering profile $I_{\mathrm{exp}}(S_j)$. $I_{\mathrm{model}}(S_j)$ represents the scattering profile of the predicted structural model. Because the GASBOR analysis does not provide a unique solution for the three-dimensional structure, 10 independent calculations were performed for each profile, and the obtained molecular models were aligned manually. The program CRYSOL (*34*) was used to calculate the scattering profiles from the atomic models of PDI.

Normal Mode Analysis. The normal mode analysis was applied to the crystal structures of yeast PDI (ref *14*, PDB entry 2B5E) and human ERp57 (ref *35*, PDB entry 3F8U) using the elastic network model (*36*, *37*). This model approximates a protein structure as an assembly of Cα atoms and springs connecting Cα-atom pairs apart within a given cutoff distance. The computation was performed using the program ELASTN coded by M. Nakasako. By performing trial calculations, the cutoff distance was selected to maximize the correlation between the thermal factors from the normal mode analysis and from those of the crystal structure. The force constant of the spring was then adjusted so as to equalize the sum of the theoretical and experimental thermal factors (*37*).

RESULTS

Preparation of PDI Samples. The SDS−PAGE patterns for the sample purified by ion-exchange chromatography after a week-long incubation demonstrated the purity and the homogeneity of the prepared PDI samples, which was also supported by the elution profiles observed in the size-exclusion and ion-exchange chromatography (data not shown). SDS−PAGE in the presence and absence of β-ME (Figure 1B) indicated that PDI in the oxidized form was free from intermolecular disulfides even after the incubation. As the reduced form of PDI was prepared through a 40 min incubation in the presence of 10 mM DTT added to PDI in the oxidized form immediately following purification by ion-exchange chromatography, the purity of the reduced form was identical to that of the oxidized form.

We confirmed that very little degradation and proteolysis occurred in the purified PDI samples by ion-exchange chromatography through comparing their observed SAXS profiles, zero-angle scattering intensities, and R_gs with those calculated for the domains and fragments which could possibly appear during degradation (Supporting Information Figure S3 and Table S1). The possibility of dimer formation in the purified PDI solutions was also excluded by comparing the experimentally obtained scattering profiles, the R_g, and $I(0,0)$ values of SAXS with those simulated from dimers found in the crystal structures of yeast PDI (*14*, *15*) (Supporting Information Figure S4 and Table S1).

We also examined whether purified PDI in the oxidized form retained substrate-binding activity. The purified PDI interacted with scrambled RNase A as demonstrated by surface plasmon resonance measurements (*17*) and could bind somatostatin, a competitive inhibitor against substrates of bovine liver PDI (*38*, *39*), as monitored by changes in the profiles and R_g values in SAXS analysis (Supporting Information Figure S5). Thus, the purified PDI in the oxidized form was shown to possess substrate-binding activity, and the substrate-binding platform was likely free from contaminants, such as small peptide fragments.

Redox State of the Active Site and Structural Cysteine Pairs. Prior to the NMR analysis, we confirmed that the secondary structure of PDI was independent of the redox conditions of the buffers by CD spectroscopy (Figure 1C). The NMR spectra for PDI under the solvent condition for rapid reduction of the active site and structural disulfides were then obtained (Figure 1D). This analysis provided a footprint of the NMR signals from the six cysteine residues of the ***a*** and ***a′*** domains in their disulfide and dithiol states. Thus, the NMR experiment revealed that the structural disulfide was maintained for approximately 5 h even in the presence of 2 mM DTT (Figure 1D).

Time-course NMR measurements were also performed to determine the redox state of the six cysteine residues under the identical buffer conditions used in the SAXS analysis (Figure 1E). Because the measurements were repeated every 40 min, the obtained NMR spectra had higher background noise than those shown in Figure 1D; however, it was possible to determine the disulfide state of the active site and non-structural cysteine pairs from the spectra shown in Figure 1D. The NMR signals of the disulfides gradually disappeared, and signals of the dithiol state arose after the addition DTT to the PDI solution (Figure 1E). The data indicated that structural disulfide Cys59−Cys66 was maintained for 40−120 min, whereas the active site disulfides of residues 30−33 and 365−368 were nearly reduced within 40 min.

On the basis of the NMR results and the CD data, we designated PDI under the oxidizing buffer conditions as the oxidized form (PDI_{ox}), and PDI incubated in the reducing buffer for 40−120 min was designated as the reduced form (PDI_{red}).

SAXS Profiles. SAXS profiles of PDI_{red} and PDI_{ox} displayed shoulders at ca. $S = 0.025$ Å^{-1} and broad maxima at ca. $S = 0.050$ Å^{-1} (Figure 2A). The profiles were qualitatively similar to that calculated from the crystal structure of yeast PDI at 277 K (*14*); however, the scattering intensities of both PDI_{red} and PDI_{ox} were significantly higher than those calculated at $S < 0.01$ Å^{-1}.

At all of the concentrations measured, the scattering intensities at $S < 0.006$ Å^{-1} increased in PDI_{ox}, whereas those at

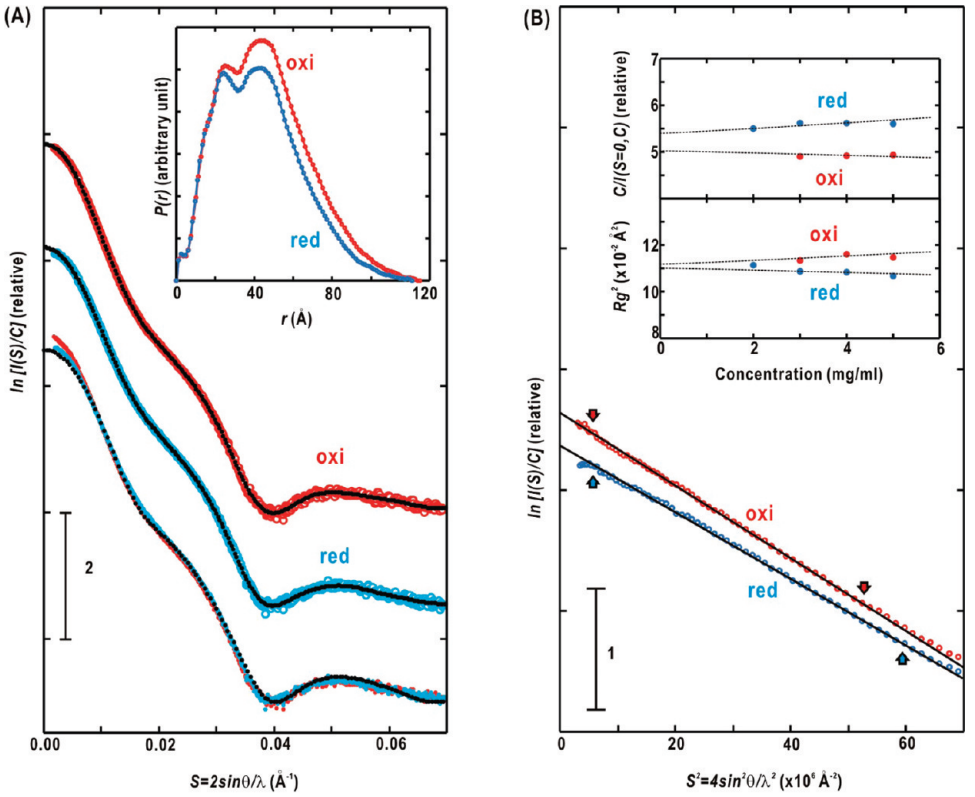

FIGURE 2: (A) SAXS profiles of PDI_{ox} (red symbols) and PDI_{red} (blue) at the dilution limit. The scattering profiles of PDI_{ox} are shifted upward for clarity. The observed profiles were compared with those calculated from the restored molecular shapes (black lines). The bottom curve compares the profiles of PDI_{ox}, PDI_{red}, and the crystal structure of yeast PDI at 277 K (black dots). The inset shows the $P(r)$ functions of PDI_{red} and PDI_{ox}. (B) Guinier plots for PDI_{ox} (red) and PDI_{red} (blue) at 4 mg/mL. The solid lines were calculated by the Guinier approximation for regions indicated by the pair of arrows. The inset shows the concentration dependencies of $C/I(0, C)$ and $R_g(C)$. The regression lines were calculated by the least-squares method.

Table 1: Molecular Weights and Structural Parameters of PDI and Fragments

	M_w from sequence (k)	M_w from SAXS (k)	$R_g(C = 0)$ (Å)	D_{max} (Å)	χ^2 values of restored models
PDI_{ox}	53.1	66.4 ± 1.6	33.4 ± 0.4	127 ± 5	1.2−1.5
PDI_{red}		58.8 ± 1.9	32.7 ± 0.7	122 ± 5	1.8−2.4

ca. $S = 0.020$ Å^{-1} decreased (Figure 2A). This increase indicated a larger apparent M_w of PDI_{ox} than that of PDI_{red}, and the decrease suggested that the rearranged domains were separated by ca. 40−50 Å according to the reciprocity between the scattering vectors and distances of the electron pairs in solute. The changes in the SAXS profile were different from those between PDI_{ox} in the presence and absence of somatostatin (Supporting Information Figure S5), suggesting that the conformations of PDI_{red}, unliganded PDI_{ox}, and liganded PDI_{ox} differed from each other.

Guinier Analysis. When the concentration of the PDI solution exceeded 6 mg/mL, scattering caused by interparticle interferences (*30*) slightly smeared the small angle region of $S < 0.005$ Å^{-1}. Thus, in the Guinier analysis, we used profiles recorded from PDI solutions with concentrations less than 6 mg/mL. The Guinier plots of both PDI_{ox} and PDI_{red} were approximated by straight lines in the region of $5 \times 10^{-6} < S^2 < 60 \times 10^{-6}$ Å^{-2}, and the calculated $C/I(S = 0,C)$ and $R_g^2(C)$ values displayed linear concentration dependencies (Figure 2B). These findings demonstrated the monodispersive properties of PDI_{red} and PDI_{ox}. The apparent M_ws of PDI_{red} and PDI_{ox} estimated from $I(S = 0,C = 0)$ were 1.1 and 1.2 times larger than that calculated from the amino acid sequence of *H. insolens* PDI, respectively (Table 1). The $R_g(C = 0)$ of PDI_{ox} differed by only ca. 1 Å from that of PDI_{red} (Table 1). The $I(S = 0,C)$ of PDI_{red} increased in proportion to C, whereas its $R_g(C)^2$ value decreased. The concentration dependencies of the two parameters were opposite in the signs between PDI_{ox} and PDI_{red}. Thus, PDI_{red} displays repulsive intersolute interactions, whereas those of PDI_{ox} are attractive.

The SAXS profiles at the infinite dilution ($S < 0.01$ Å^{-1}) and that from the 10 mg/mL PDI solution with good statistics ($S > 0.01$ Å^{-1}) were merged for the following analyses. The $P(r)$ functions of PDI_{ox} and PDI_{red} had two maxima at ca. 25 and 45 Å, corresponding to the center-to-center distances among the four domains and monotonously decreased to the maximum dimensions (D_{max}) (Figure 2A and Table 1), which only differed by 5 Å between PDI_{ox} and PDI_{red}. Due to the increase in the apparent M_w of PDI_{ox}, the $P(r)$ of PDI_{ox} took higher values than that of PDI_{red}.

Low-Resolution Molecular Models of PDI_{red} and PDI_{ox}. The restored molecular models of both PDI_{red} and PDI_{ox} appeared as "y" shapes (Figure 3A) and reproduced the experimental profiles (Figure 2A), as indicated by the χ^2 values

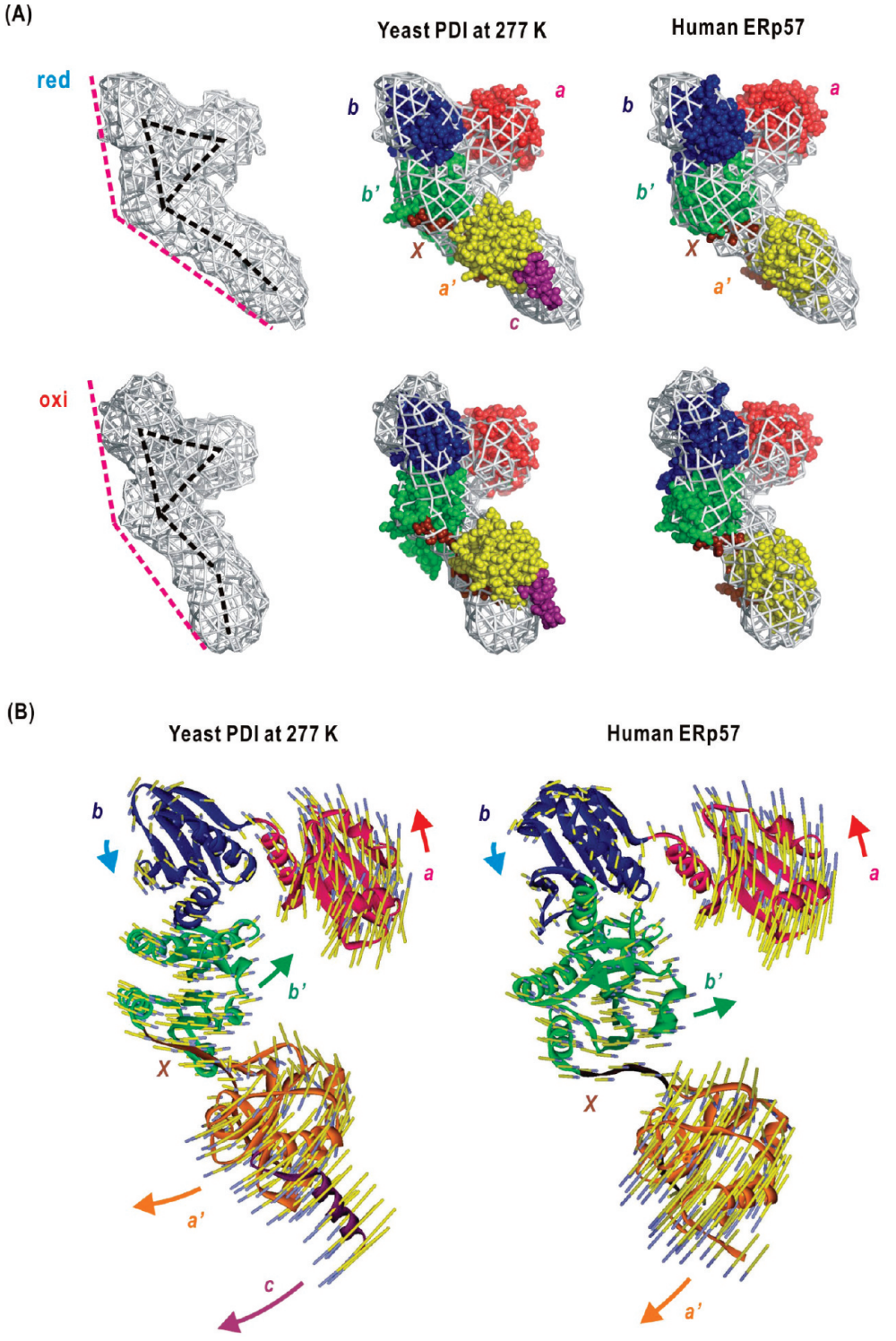

FIGURE 3: (A) Molecular shapes of PDI_{red} and PDI_{ox} restored from the SAXS profiles are shown by the densities of dummy residues in $4 \times 4 \times 4$ Å^3 cubes after superimposing 10 independently restored models that were aligned so as to optimally overlap. The black dashed lines trace the high-density region, and the pink dashed lines help to illustrate the redox-dependent structural differences. The molecular models were compared with the crystal structures of yeast PDI at 277 K (PDB ID 2B5E (*14*)) and human ERp57 (3F8U (*35*)) and were manually fitted to the molecular shape so that the ***a*–*b*–*b*′** region fit to the triangular-shaped part. The crystal structures are shown as space-filling models, and the domains are colored according to the scheme in Figure 1A. This panel was prepared using PyMol (*54*). (B) Illustration of the normal mode motions with the lowest energy in the crystal structures of yeast PDI at 277 K (*14*) and ERp57 (*34*). The 10 times magnified amplitudes of the motions are illustrated by colored sticks, which indicate the directions of the motions from the yellow to the blue ends. The cutoff distance applied in each calculation was 15 Å.

(Table 1). The number of dummy residues necessary to reproduce the profile of PDI_{ox} (500 dummy residues) was ca. 1.1 times larger than that for PDI_{red} (450 dummy residues). This ratio correlated with the discrepancy in the apparent M_ws of PDI_{red} and PDI_{ox} estimated by the Guinier analysis (Table 1). The molecular models were similar to the SAXS model of human ERp57 (*40*), and the crystal structures of yeast PDI at 277 K (*14*) and human ERp57 in the liganded form (*35*), but were distinct

from the SAXS models of human ERp72 (*41*) and human PDI (*42*).

Each molecular model was roughly divided into two parts: one consisted of a triangular assembly of three globular domains with approximate diameters of 25 Å and the other formed an ellipsoid shape ca. 40 Å long and 25 Å wide. The triangular cluster was modeled as the ***a*−*b*−*b*′** region, and the ellipsoid was assigned to the ***a*′−*c*** region by referring to the reported crystal structures of yeast PDI at 277 K (*14*) and human ERp57 (*35*). In PDI_{ox}, the position and orientation of the ***a*′−*c*** region relative to the ***a*−*b*−*b*′** region were distinct from those in PDI_{red}, suggesting a redox-dependent rearrangement of these two regions.

It was difficult to simultaneously overlap the four domains in the crystal structure of yeast PDI at 277 K in any orientation on the SAXS models. When the ***a*−*b*−*b*′** region of the crystal structure was optimally superimposed to the triangular assembly, the ***a*′−*c*** region did not overlap with the ellipsoid parts of PDI_{red} and PDI_{ox} (Figure 3A). In contrast, the four thioredoxin domains in the crystal structure of ERp57 fitted the molecular model of PDI_{ox} better than those of yeast PDI (Figure 3A).

Normal Mode Analysis. Normal mode analyses on the crystal structures of yeast PDI (*14*) and ERp57 (*34*) provided clues for understanding the inherent intermolecular motions in the restored modular structures (Figure 3B). In the lowest mode, the ***a***, ***b***, and ***b*′** domains rotated collectively around the center of the ***a*−*b*-*b*′** region, and the ***a*′−*c*** region rotated around the ***x***-linker region in an antiphase against the movement of the ***a*−*b*−*b*′** region. This antiphase movement was likely intrinsic in the modular structure and was advantageous for changing the solvent accessibility of the primary substrate-binding platform in the ***b*′** domain.

DISCUSSION

The SAXS analyses of spectroscopically and biochemically characterized PDI samples (Figure 1) suggested a redox-dependent rearrangement of the ***a*′−*c*** region relative to the ***a*−*b*−*b*′** region (Figures 2 and 3) and quantitatively demonstrated changes in the apparent M_ws in keeping with the molecular dimensions indicated by the R_g and D_{max} (Figure 2 and Table 1). On the basis of these experimental findings, we here discuss the mechanisms in redox-dependent conformational and solvation changes.

*Flexibility of the **x**-Linker Region*. The present SAXS data revealed full-length PDI undergoes redox-dependent conformational changes, particularly in the ***a*′−*c*** region. In our previous SAXS and NMR study on the ***b*′−*X*−*a*′** fragment of *H. insolens* (*17*), the arrangement and hydration of the domains were dependent on the redox state of the ***a*′** active site, whereas those of the ***a*−*b*** fragment were nearly independent of the redox state of the ***a*′** active site. Thus, in both the full-length and truncated fragments of PDI, the oxidation of the ***a*′** active site likely induces movements of the ***a*′** domains to increase the solvent accessibility of the hydrophobic surface of the ***b*′** domain. For this movement, the conformational flexibility of the ***x***-linker region is likely necessary, as predicted from the normal modes inherent in the modular structure of PDI (Figure 3B).

Conformational flexibility of the ***x***-linker region has been reported to be critical for substrate-binding site accessibility in both yeast and human PDIs. For example, the ***x***-linker region of yeast PDI displays different conformations in two crystal forms (*14*, *15*), and solvent accessibility to the ***b*′** domain in human PDI is modulated by the alternative conformations of the ***x***-linker region (*43*). In addition, the C-terminal region of ERp44, corresponding to the ***x***-linker regions of human PDI, *H. insolens* PDI, and human ERp57, displays a reversible capping of the substrate binding site located in its ***b*′** domain (*44*). Considering the high sequence identity of the ***x***-linker regions among yeast and *H. insolens* PDIs and human ERp57 (Figure 1A), these experimental findings suggest that the conformational flexibility of the ***x***-linker region is likely a common characteristic in these three proteins.

In yeast PDI, the ***a***, ***b*′**, and ***a*′** domains are reported to work cooperatively (*45*). The ***a*′** and ***b*′** domains have predominant roles for substrate binding, although all four thioredoxin domains are required for the function of the enzyme (*19*). On inspection of the crystal structures of yeast PDI (*14*) and human ERp57 (*35*), the flexible ***x***-linker appears to be necessary for the movement of the ***a*′** domain to alter the solvent accessibility of the substrate-binding surface of the ***b*′** domain, whereas the movement of the ***a*** and ***b*** domains would be restricted by the short loop connecting them. In *H. insolens* PDI, the ***b*′−*X*−*a*′** fragment acts as the major substrate-binding site, with the ***a*−*b*** region supporting the binding (*17*). This is similar to the case for human PDI, as the ***b*′−*X*−*a*′** region fulfills the minimum requirement for the substrate-binding function, and the ***a*−*b*** region enhances the function (*46*). Therefore, the flexibility of the ***x***-linker may be relevant to the asymmetry regarding the conformational flexibility between the ***a*−*b*** and ***a*′−*x*−*b*′** regions in full-length PDIs. Concerning the ***b*′−*x*** fragment of human PDI, mutational studies of its ***x***-linker region have revealed the possibility that the linker modulates the exposure of the substrate-binding surface of the ***b*′** domain (*43*). Although the current knowledge on the effects of mutations is still limited to the non-native fragment, systematic mutational studies of the ***x***-linker residues in full-length PDIs will be helpful to further understand the role of the linker in the conformational flexibility of PDI.

Redox-Dependent Solvation Changes. The apparent M_ws of PDI_{red} and PDI_{ox} were larger than those calculated from the amino acid sequence (Table 1). The discrepancies are enhanced depending on the types of additive ions and reagents present in the buffers (Supporting Information Figure 1). With respect to human PDI, the reported SAXS M_w of 69K is 1.2 times larger than the M_w calculated from the amino acid sequence (57K) (*42*). Because the M_w from SAXS analysis reflects the sum of the electron densities in a solute, this inconsistency can be attributed to solvation. When solvation clusters or shells have higher electron densities than the bulk solvent, the resulting SAXS profiles are smeared (*47*, *48*). For instance, yeast PDI at 277 K with an accessible solvent area of 26000 $Å^2$ is able to associate with 1300 hydration water molecules, when assuming the average area (ca. 20 $Å^2$) is covered by one hydration water molecule in a monolayer hydration of soluble proteins (*49*). The discrepancies in the M_ws of PDI_{red} and PDI_{ox} correspond to ca. 300 and 700 hydration water molecules, respectively. As the contribution of hydration water or solvent molecules to the scattering profile depends on their mobility on the protein surface, hydration water or solvent molecules causing an increase in the M_w are considered to have low mobility, and the monolayer hydration shell therefore likely comprises mobile solvent molecules.

Because $R_g(C = 0)$ is the second moment of electron density distribution within a solute, it is insensitive to changes in electron densities at the central region of a solute. This general characteristic of R_g allows us to speculate that PDI_{ox}, and likely

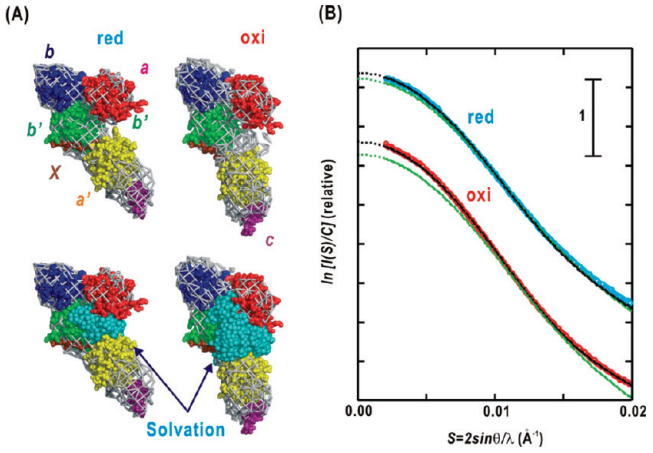

FIGURE 4: (A) Putative PDI_{red} and PDI_{ox} models without (top) or with (bottom) solvation in the cleft formed by the four thioredoxin domains. The ***a***, ***b***, ***b′***, and ***a′*** domains were separately and manually fitted to the SAXS models. In the solvated models, water molecules (cyan-colored spheres) taken from a snapshot of a molecular dynamics simulation (*55*) were set in the cleft so as to avoid fatal overlaps with the domains. The numbers of water molecules in the PDI_{red} and PDI_{ox} models were adjusted to 300 and 700, respectively, as predicted from their apparent M_w values. This panel was prepared using PyMol (*54*). (B) The scattering curves of the models without (green dotted lines) and with (black lines) hydration water molecules in the cleft were compared with the observed profiles of PDI_{red} (cyan) and PDI_{ox} (red). The R_g values of the PDI_{ox} and PDI_{ox} models without water molecules were 32.0 and 31.2 Å, respectively. The "simulated hydration" of the active site cleft contributed slightly to the increase of R_g values of the PDI_{ox} (33.1 Å) and PDI_{red} (32.0 Å) models.

PDI_{red}, adsorbs solvent molecules at the molecular center located at the substrate-binding cleft formed by the four thioredoxin domains. The ***b′*−*X*−*a′*** fragment in the oxidized form has an apparent M_w that is 1.1 times larger than that in the reduced form, whereas the M_w of the ***a*−*b*** fragment is independent of the redox state (*17*). Thus, the surfaces of the ***b′*** and ***a′*** domains would provide the solvation platform in PDI.

Figure 4A shows putative models for "solvated" PDI_{red} and PDI_{ox}. In these models, water molecules representing solvation are set on the mastoparan-binding surface of the ***b′*−*X*−*a′*** region, which was identified by our NMR analysis (*17*). The solvated models reproduce the experimental SAXS profiles in $S < 0.02$ Å^{-1} and R_g values much better than those without water molecules. Thus, the redox-dependent alternation of SAXS profiles is likely a result of not only the rearrangement of the ***a′*−*c*** region, but also by the solvation change on the surface of the ***b′*−*a′*** region.

The hydration of hydrophobic protein surfaces, such as the ***b′*** domain, is under active investigation, but the process is known to be distinct from that surrounding polar protein atoms (*50*). Oligomeric clusters of water molecules are suspended on hydrophobic surfaces through van der Waals contacts with apolar atom groups and are anchored by hydrogen bonds to polar protein atoms surrounding the surfaces (*51*). The relevance of hydrophobic hydration to the observed redox-dependent conformational changes in PDI is discussed in the following section.

How Does the Redox Change in the ***a′*** *Active Site Affect the Dynamics of the* ***b′*** *Domain?*. In several PDIs, the redox state of the ***a′*** domain appears to influence the dynamics of the ***b′*** domain. For instance, mutations destabilizing the ***a′*** domain in human PDI alter the peptide-binding activity that is presumably conducted by the ***b′*** domain (*52*). Although several ideas have been proposed to explain how the redox state of the ***a′*** active site regulates the dynamics of the ***b′*** domain, it is considered that conformational changes in the active site upon oxidation decrease the conformational flexibility of the ***b′*** domain (*5*).

In the ***a′*−*X*−*b′*** fragment of *H. insolens* PDI, oxidation of the ***a′*** domain induces changes in the dynamics of the ***b′*** domain, as revealed by NMR measurements of the hydrogen−deuterium exchange and R_2 relaxation rates (*17*). In the reduced form, signals of the nuclear Overhauser effect between the ***a′*** and ***b′*** domains are difficult to detect (unpublished data). In the present SAXS study, we observed the redox-dependent movement of the ***a′*−*c*** region; however, the ***a′*** active site is at a distance of greater than 23 Å from the mastoparan-binding region in the putative model presented in Figure 4A. Although the altered dynamics surrounding the ***a′*** active site may be a predominant factor for regulating the dynamics of the ***b′*** domain, we could not deny the possibility that the redox-dependent solvation/hydration changes upon oxidation of PDI influence the dynamics of the ***b′*** domain, similar to the hydration-controlled domain motions observed in certain enzymes (*50*, *53*).

On the basis of the hydration changes in PDI, we propose the following scenario for the observed dynamics of the ***b′*** domain induced by the oxidation of the ***a′*** active site. Oxidation of the ***a′*** active site alters the surface property from a hydrophilic dithiol in the reduced form to a hydrophobic disulfide under the influence of histidine (*17*). This change likely requires reorganization of the hydration from a hydrophilic to hydrophobic mode (*50*). Such a reorganization may assist to transmit the redox change in the active site to a marginal part of the ***b′*** domain located near the ***a′*** domain. This hypothetical mechanism could be examined in future studies by monitoring the structural changes induced by hydration in the cleft of PDI using spectroscopic techniques.

ACKNOWLEDGMENT

We are grateful to Drs. Osamu Asami and Tsutomu Kajino of Toyota Central Research and Development Laboratory for kindly providing plasmid vectors containing the cDNA of the fungal PDI. We thank Kiyomi Senda and Kumiko Hattori of Nagoya City University for help in the preparation of the recombinant proteins. We also thank Drs. Masaki Yamamoto, Katsuaki Inoue, Kazuki Ito, and Takaaki Hikima for support in the SAXS experiments at the SPring-8 facility and Dr. Shinya Hanashima of RIKEN for help with NMR measurements. We finally thank to Dr. Greg Newton for kind and valuable comments in editing our manuscript.

SUPPORTING INFORMATION AVAILABLE

SAXS experiments on PDI in four types of buffers, CD spectra of PDI in three types of buffers, theoretical scattering curves and R_g values of fragments and domains of PDIs, and SAXS experiments on PDI in the presence of somatostatin. This material is available free of charge via the Internet at http://pubs.acs.org.

REFERENCES

1. Frand, A. R., Cuozzo, J. W., and Kaiser, C. A. (2000) Pathways for protein disulfide bond formation. *Trends Cell Biol. 10*, 203–210.
2. Xiao, R., Wilkinson, B., Solovyov, A., Winther, J. R., Holmgren, A., Lundström-Ljung, J., and Gilbert, H. F. (2004) The contribution of protein disulfide isomerase and its homologous to oxidative protein folding in the yeast endoplasmic reticulum. *J. Biol. Chem. 279*, 49780–49786.

3. Wilkinson, B., and Gilbert, H. F. (2004) Protein disulfide isomerase. *Biochim. Biophys. Acta 1699*, 35–44.
4. Gruber, C. W., Čemažar, Heras, B., Martin, J. L., and Craik, D. J. (2006) Protein disulfide isomerase: the structure of oxidative folding. *Trends Biochem. Sci. 31*, 455–464.
5. Hatahet, F., and Ruddock, L. W. (2009) Protein disulfide isomerase: a critical evaluation of its function in disulfide bond formation. *Antioxid. Redox Signal. 11*, 2807–2850.
6. Wang, C. C., and Tsou, C. L. (1993) Protein disulfide isomerase is both an enzyme and a chaperone. *FASEB J. 7*, 1515–1517.
7. Winter, J., Klappa, P., Freedman, R. B., Lilie, H., and Rudolph, R. (2002) Catalytic activity and chaperone function of human protein-disulfide isomerase are required for the efficient refolding of proinsulin. *J. Biol. Chem. 277*, 310–317.
8. Edman, J. C., Ellis, L., Blacher, R. W., Roth, R. A., and Rutter, W. J. (1985) Sequence of protein disulphide isomerase and implications of its relationship to thioredoxin. *Nature 317*, 267–270.
9. Ferrari, D. M., and Söling, H.-D. (1999) The protein disulfide-isomerase family: unraveling a string of folds. *Biochem. J. 339*, 1–10.
10. Darby, N. J., Kemmink, J., and Creighton, T. E. (1996) Identifying and characterizing a structural domain of protein disulfide isomerase. *Biochemistry 35*, 10517–10528.
11. Kemmink, J., Darby, N. J., Dijkstra, K., Nilges, M., and Creighton, T. E. (1996) Structure determination of the N-terminal thioredoxin-like domain of protein disulfide isomerase using multidimensional heteronuclear $^{13}C/^{15}N$ NMR spectroscopy. *Biochemistry 35*, 7684–7691.
12. Kemmink, J., Dijkstra, K., Mariani, M., Scheek, R. M., Penka, E., Nilges, M., and Darby, N. J. (1999) The structure in solution of the b domains of protein disulfide isomerase. *J. Biomol. NMR 13*, 357–368.
13. Nakano, M., Murakami, C., Yamaguchi, Y., Sasakawa, H., Harada, T., Kurimoto, E., Asami, O., Kajino, T., and Kato, K. (2006) NMR assignments of the b′ and a′ domains of thermophilic fungal protein disulfide isomerase. *J. Biomol. NMR 36*, 44.
14. Tian, G., Xiang, S., Novia, R., Lennarz, W. J., and Shindelin, H. (2006) The crystal structure of yeast protein disulfide isomerase suggests cooperativity between its active sites. *Cell 124*, 61–73.
15. Tian, G., Kober, F.-X., Lewandrowski, U., Sickmann, A., Lennarz, W. J., and Schindelin, H. (2008) The catalytic activity of protein-disulfide isomerase requires a conformationally flexible molecule. *J. Biol. Chem. 283*, 33630–33640.
16. Denisov, A. Y., Määttänen, P., Dabrowski, C., Kozlov, G., Thomas, D. Y., and Gehring, K. (2009) Solution structure of the bb′ domains of human protein disulfide isomerase. *FEBS J. 276*, 1440–1449.
17. Serve, O., Kamiya, Y., Maeno, A., Nakano, M., Murakami, C., Sasakawa, H., Yamaguchi, Y., Harada, T., Kurimoto, E., Yagi-Utsumi, M., Iguchi, T., Inaba, K., Kikuchi, J., Asami, O., Kajino, T., Oka, T., Nakasako, M., and Kato, K. (2010) Redox-dependent domain rearrangement of protein disulfide isomerase coupled with exposure of its substrate-binding hydrophobic surface. *J. Mol. Biol. 396*, 361–374.
18. Lyles, M. M., and Gilbert, H. F. (1994) Mutations in the thioredoxin sites of protein disulfide isomerase reveal functional nonequivalence of the N- and C-terminal domains. *J. Biol. Chem. 269*, 30946–30952.
19. Klappa, P., Ruddock, L. W., Darby, N. J., and Freedman, R. B. (1998) The b′ domain provides the principal peptide-binding site of protein disulfide isomerase but all domains contribute to binding of misfolded proteins. *EMBO J. 17*, 927–935.
20. Darby, N. J., Penka, E., and Vincentelli, R. (1998) The multi-domain structure of protein disulfide isomerase is essential for high catalytic efficiency. *J. Mol. Biol. 276*, 239–247.
21. Kulp, M. S., Frickel, E.-M., Ellgaard, L., and Weissman, J. S. (2006) Domain architecture of protein-disulfide isomerase facilitates its dual role as an oxidase and an isomerase in Ero1p-mediated disulfide formation. *J. Biol. Chem. 281*, 876–884.
22. Cheung, P. Y., and Churchich, J. E. (1999) Recognition of protein substrates by protein-disulfide isomerase: a sequence of the b′ domain responds to substrate binding. *J. Biol. Chem. 274*, 32757–32761.
23. Pirneskoski, A., Klappa, P., Lobell, M., Williamson, R. A., Byrnet, L., Alanen, H. I., Salo, K. E. H., Kivirikko, K. I., Freedman, R. B., and Ruddock, L. W. (2004) Molecular characterization of the principal substrate binding site of the ubiquitous folding catalyst protein disulfide isomerase. *J. Biol. Chem. 279*, 10374–10381.
24. Tsai, B., Rodighiero, C., Lencer, W. I., and Rapoport, T. A. (2001) Protein disulfide isomerase acts as a redox-dependent chaperone to unfold cholera toxin. *Cell 104*, 937–948.
25. Lumb, R. A., and Bulleid, N. J. (2002) Is protein disulfide isomerase a redox-dependent molecular chaperone? *EMBO J. 21*, 6763–6770.
26. Kajino, T., Miyazaki, C., Asami, O., Hirai, M., Yamada, Y., and Udaka, S. (1998) Thermophilic fungal protein disulfide isomerase. *Methods Enzymol. 290*, 50–59.
27. Kajino, T., Sarai, K., Imaeda, T., Idekoba, C., Asami, O., Yamada, Y., Hirai, M., and Udaka, S. (1994) Molecular cloning of a fungal cDNA encoding protein disulfide isomerase. *Biosci., Biotechnol., Biochem. 58*, 1424–1429.
28. Wilkinson, B., Xiao, R., and Gilbert, H. F. (2005) A structural disulfide of yeast protein-disulfide isomerase destabilizes the active site disulfide of the N-terminal thioredoxin domain. *J. Biol. Chem. 280*, 11483–11487.
29. Kato, K., Matsunaga, C., Igarashi, T., Kim, H.-H., Odaka, A., Shimada, I., and Arata, Y. (1991) Complete assignment of the methionyl carbonyl carbon resonances in switch variant anti-dansyl antibodies labeled with [1-^{13}C]methionine. *Biochemistry 30*, 270–278.
30. Nakasako, M., Iwata, T., Matsuoka, D., and Tokutomi, S. (2004) Light-induced structural changes of LOV-domain containing polypeptides from *Arabidopsis* phototropin 1 and 2 studied by small-angle X-ray scattering. *Biochemistry 43*, 14881–14890.
31. Guinier, A., and Fournet, G. (1955). Small-Angle Scattering of X-rays, John Wiley, New York.
32. Svergun, D. I. (1992) Determination of regularization parameter in indirect-transform methods using perceptual criteria. *J. Appl. Crystallogr. 25*, 495–503.
33. Svergun, D. I. (1999) Restoring low resolution structure of biological macromolecules from solution scattering using simulated annealing. *Biophys. J. 76*, 2879–2886.
34. Svergun, D. I., Barberato, C., and Koch, M. H. J. (1995) CRYSOL a program to evaluate X-ray solution scattering of biological macromolecules from atomic coordinates. *J. Appl. Crystallogr. 28*, 768–773.
35. Dong, G., Wearsch, P. A., Peaper, D. R., Cresswell, P., and Reinisch, K. M. (2009) Insights into MHC class I peptide loading from the structure of the tapasin-ERp57 thiol oxidoreductase heterodimer. *Immunity 30*, 21–32.
36. Tirion, M. M. (1996) Large amplitude elastic motions in proteins from a single-parameter, atomic analysis. *Phys. Rev. Lett. 77*, 1905–1908.
37. Tama, F., Gadae, F. X., Marques, O., and Sanejouand, Y. (2000) Building block approach for determining low-frequency normal modes of macromolecules. *Proteins: Struct., Funct., Genet. 41*, 1–7.
38. Morjana, N. A., and Gilbert, H. F. (1991) Effect of protein and peptide inhibitors on the activity of protein disulfide isomerase. *Biochemistry 30*, 4985–4990.
39. Klappa, P., Hawkins, H. C., and Freedman, R. B. (1997) Interactions between protein disulfide isomerase and peptides. *Eur. J. Biochem. 248*, 47–42.
40. Kozlov, G., Määttänen, P., Schrag, J. D., Pollock, S., Cygler, M., Nagar, B., Thomas, D. Y., and Gehring, K. (2006) Crystal structure of the bb′ domains of protein disulfide isomerase ERp57. *Structure 14*, 1331–1339.
41. Kozlov, G., Määttänen, P., Schrag, J. D., Hura, G. L., Gabrielli, L., Cygler, M., Thomas, D. Y., and Gehring, K. (2009) Structure of the noncatalytic domains and global fold of the protein disulfide isomerase ERp72. *Structure 17*, 651–659.
42. Li, S.-j., Hong, X.-g., Shi, Y.-y., Li, H., and Wang, C.-c. (2006) Annular arrangement and collaborative actions of four domains of protein disulfide isomerase: a small-angle X-ray scattering study in solution. *J. Biol. Chem. 281*, 6581–6588.
43. Nguyen, V. D., Wallis, K., Howard, M. J., Haapalainen, A. M., Salo, K. E. H., Saaranen, M. J., Sidhu, A., Wierenga, R. K., Freedman, R. B., Ruddock, L. W., and Williamson, R. A. (2008) Alternative conformations of the x region of human protein disulfide isomerase modulate exposure of the substrate binding b′ domain. *J. Mol. Biol. 383*, 1144–1155.
44. Wang, L., Wang, L., Vavassori, S., Li, S., Ke, H., Anelli, T., Degano, M., Ronzoni, R., Sitia, R., Sun, F, and Wang, C.-c. (2008) Crystal structure of human ERp44 shows a dynamics functional modulation by its carboxy-terminal tail. *EMBO Rep. 9*, 642–647.
45. Koivunen, P., Salo, K. E. H., Myllyharju, J., and Ruddock, L. W. (2005) Three binding sites in protein-disulfide isomerase cooperate in collagen prolyl 4-hydroxylase tetramer assembly. *J. Biol. Chem. 280*, 5227–5235.
46. Pireneskoski, A., Ruddock, L. W., Klappa, P., Freedman, R. B., Kivirikko, K. I., and Koivunen, P. (2001) Domains *b′* and *a′* of protein disulfide isomerase fulfill minimum requirement for function as a subunit of prolyl 4-hydroxyalase: the N-terminal domains *a* and *b* enhance this function and can be substituted in part by those of ERp57. *J. Biol. Chem. 276*, 11287–11293.

47. Ibel, K., and Stuhrmann, H. B. (1975) Comparison of neutron and X-ray scattering of dilute myoglobin solutions. *J. Mol. Biol. 93*, 255–265.
48. Svergun, D. I., Richard, S., Koch, M. H. J., Sayer, Z., Kuprin, S, and Zaccai, G. (1998) Protein hydration in solution: experimental observation by x-ray and neutron scattering. *Proc. Natl. Acad. Sci. U.S.A. 95*, 2267–2272.
49. Nakasako, M. (2001) Large-scale networks of hydration water molecules around proteins investigated by cryogenic X-ray crystallography. *Cell. Mol. Biol. 47*, 767–790.
50. Nakasako, M. (2004) Water-protein interactions from high-resolution protein crystallography. *Philos. Trans. R. Soc. London B359*, 1191–1206.
51. Higo, J., Kono, H., Nakamura, H., and Sarai, A. (2000) Solvent density and long-range dipole field around a DNA-binding protein studied by molecular dynamics. *Proteins: Struct., Funct., Genet. 40*, 193–206.
52. Klappa, P., Koivunen, P., Pirneskoski, A., Karvonen, P., Ruddock, L. W., Kivirikko, K. I., and Freedman, R. B. (2000) Mutations that destabilize the a′ domain of human protein-disulfide isomerase indirectly affect peptide binding. *J. Biol. Chem. 275*, 13213–13218.
53. Nakasako, M., Fujisawa, T., Adachi, S., Kudo, T., and Higuchi, S. (2001) Large-scale domain movements and hydration structure changes in the active-site cleft in unligated glutamate dehydrogenase from *Thermococcus profundus* studied by cryogenic X-ray crystal structure analysis and small-angle X-ray scattering. *Biochemistry 40*, 3069–3079.
54. DeLano, W. L. (2002) The PyMOL Molecular Graphics System, DeLano Scientific, Palo Alto, CA (available at http://www.pymol.org).
55. Higo, J., and Nakasako, M. (2002) Hydration structure of human lysozyme investigated by molecular dynamics simulation and cryogenic X-ray crystal structure analyses: on the correlation between and crystal-water sites, solvent-density and solvent-dipole. *J. Comput. Chem. 23*, 1323–1336.